Supplementary Information for

A COF-like Conductive Conjugated Microporous Poly(aniline) Serving as Current Collector Modifier for High-Performance Li-S Batteries

Xin Chen, ‡ [a, c] Yubing Wang, ‡ [a] Jianan Wang, [a, c, *] Jianwei Liu, [a, c] Shiyi Sun, [a] Lei Zhu, [a, d] Qianyue Ma, [a] Ningrui Zhu, [e] Xi Wang, [a] Jie Chen, [b, *] Wei Yan [a, *]

[a] Department of Environmental Science and Engineering, State Key Laboratory of Multiphase Flow in Power Engineering, Xi'an Jiaotong University, 28 Xianning West Road, Xi'an 710049, China

[b] School of Environmental and Safety Engineering, Fuzhou University, 2 Xueyuan Road, Fuzhou, 350108, China

[c] Zhejiang Research Institute of Xi'an Jiaotong University, 328 Wenming Road, Hangzhou 310000, China

[d] School of Physics and Electrical Engineering, Weinan Normal University, Chaoyang Street, Weinan, 714099, China

[e] College of Arts College of Landscape Architecture, Fujian Agriculture and Forestry University, 63 xiyuangong Road, Fuzhou, 350108, China

‡ These authors contributed equally to this work.

*** Corresponding author.**

E-mail address: wangjn116@xjtu.edu.cn (Jianan Wang);

jiechen@fzu.edu.cn (Jie Chen),

yanwei@xjtu.edu.cn (Wei Yan).

Table of Contents

Supplementary Experimental Section

1. Chemicals and materials

All chemicals were of analytical grade and used without further purification.

Tris(4-bromophenyl) amine, phenylenediamine, bis(dibenzylideneacetone)-palladium(0) (Pd-$(dba)_2$); 2-dicyclohexylphosphino-2′,4′,6′-triisopropylbiphenyl (XPhos, 97%); sodium tert-butoxide (NaOtBu, 97%), Polyacrylonitrile (PAN, average M_w=150000), dimethylformamide (DMF), lithium sulfide (Li_2S) was obtained from Sigma-Aldrich. sodium fluoride (NaF) , sodium dodecyl benzenesulfonate (SDS) Aniline (99.5%)(was distilled under reduced pressure, and stored in darkness at 0 °C under N_2 atmosphere prior), Iron (Ⅲ) chloride anhydrous ($FeCl_3$), ammonium persulfate ($(NH_4)_2S_2O_8$), hydrochloric acid (HCl, 37%) were purchased from Sinopharm Chemical Reagent Co., Ltd. Poly(vinylidene fluride-co-hexafluoropropylene) (PVDF-HFP, average M_w=400000) was obtained from Macklin. Sublimed sulfur (S) and N-methyl-2-pyrrolidone (NMP) was obtained from Aladdin. Carbon nanotubes (CNTs) were obtained from Nanjing XFNANO Materials Tech Co. Ltd. Lithium foils were obtained from Tianjin Zhongneng Lithium Industry Co.Ltd. The PP separator is Celgard 2500 (America).

2. Preparation of CNF/CMPA/S cathode

2.1 Preparation of CMPA

CMPA was synthesized using Buchwald-Hartwig (BH) coupling reaction as reported in our previous paper. A core of tris(4-bromophenyl)amine (0.5 mmol), a linker of phenylenediamine (0.5 mmol to acquire the 1:1 ratio of core to linker), XPhos (0.045 mmol), $Pd(dba)_2$ (0.04 mmol, 4 mol %), NaOtBu (3.5 mmol), and the BXJ salt NaF (0.5 mmol) were inserted with nitrogen gas. Anhydrous tetrahydrofuran (THF) (30 mL) was thereafter added under the nitrogen atmosphere. The reaction mixture was then heated with a hot plate under stirring at 65 ℃. After 48 h, the mixture was cooled to room temperature. The products were further purified with 200 mL of $CHCl_3$, ethanol,

methanol, and boiling water to remove the catalyst, impurities, and oligomers, followed by a 72 h Soxhlet extraction (each 24 h for methanol, THF and chloroform in order). The average yields of CMPA reached 99.32%. The final products were rinsed with distilled water and ethanol, and then vacuum dried at 60 °C for 48 h.

2.2 Preparation of PANi

PANi was synthesized using a one-pot chemical oxidative polymerization method. 6.75g $FeCl_3$ particles were dissolved in 100 mL solution of HCl (0.1 mol/L) in a three-necked flask. After magnetic stirring for 0.5 h, aniline (5 mL) monomer was added to the suspension liquid and stirred for 1 h. Then, ammonium persulphate (APS) solid was added to the mixture slowly under mechanical stirring and the polymerization reaction lasted for another 12 h under 30 ℃ temperature. The collected precipitates were rinsed with distilled water and ethanol, and then dried at 60 °C for 48 h.

2.3 Preparation of carbon nanofibers (CNFs)

The PAN nanofibers membrane was prepared via an electrospinning method as reported in our previous paper [1].

2.4 Preparation for CNF/CMPA (CNF/PANi) membrane

1 g PVDF-HFP solid was dissolved in 10 mL NMP by magnetically stirring at 60 °C for 6 h to form binder solution. 2 ml PVDF-HFP solution mix with 30 mg CMPA powder and ball-milling it at room temperature for 3 h. The slurry is evenly coated on the weighing carbon nanofiber membrances, then, put them into a vacuum oven and heated for 6 h at 60 °C. According to the above methods, PANi-modified membrance can be prepared, which will not be described here.

2.5 Preparation for CNF/CMPA/S (CNF/PANi/S) electrodes

280 mg sulfur powder and 80mg carbon nanotubes were mixed in a ball mill tank, 0.4 mL PVDF-HFP solution was added (the weight ratio of S, C and Binder was 7:2:1) and ball mashed for 3 h to obtain active slurry. Subsequently, the slurry was evenly coated on modified carbon nanofibers (CNF/CMPA or CNF/PANI) and kept them into a vacuum oven at 60 °C for 10 h.

3. Characterization

Field emission scanning electron microscopy (SEM) images and mapping were

obtained using a GeminiSEM 500 (China) microscope. The Fourier transform infrared (FTIR) spectra were obtained by the KBr pellet method on a BRUKER TENSOR 37 FTIR (Germany) spectrophotometer in the region between 1000 and 4000 cm^{-1}. X-ray diffraction (XRD) was performed on a SHIMADZU XRD-6000 using Cu Kα radiation from 10° to 80°. Brunauer-Emmett-Teller (BET) specific surface areas and pore distributions were acquired by JW-BK200B JWGB (China) at liquid nitrogen temperature (-196 °C) using. X-ray photoelectron spectroscopy (XPS) measurements were carried out on a Kratos Axis Ultra (England) instrument using monochromatic Al Ka radiation (150 W, 15 kV and 1486.6 eV) at 10^{-9} Torr. Binding energies were calibrated relative to the C 1s peak (284.8 eV). Thermogravimetric analysis (TGA) was performed on a TG-DTG-60FTIR (China) apparatus with a heating rate of 10 $^{o}C\ min^{-1}$ from room temperature to 800 °C under Nitrogen atmosphere. The ultraviolet-visible (UV-vis) spectra were measured by a Shimadzu UV2600A (Japan) UV-visible spectrophotometer in the wavelength range of 300-900 nm with deionized water as a reference sample. The S content of the lithium metal anodes (after cycles) was analyzed by inductively coupled plasma-atomic emission spectrometry (ICP-AES) on a Shimadzu ICPE-9000 (Japan) instrument.

4. Li-S cell assembly and electrochemical measurements

The Li-S coin type (2032) cell was assembled by using a free-standing CNF/CMPA/S, CNF/PANi/S and CNF/S as cathodes, PP (Celgard 2500) as a separator, and Li metal (thickness is 200 μm) as an anode in an Ar-filled glovebox (Dellix LS750S, China) with moisture and oxygen contents below 0.5 ppm. The electrolyte was composed of 1.0 M lithium bis(trifluoromethanesulfonyl) imide (LITFSI) in a solvent mixture of DME/DOL (1 : 1 by volume) with 1.0 % $LiNO_3$ additive. The quantity of electrolyte was controlled at 15~20 μL per 1 mg sulfur. Galvanostatic charge–discharge tests were studied by a LANHE (China) battery tester within a voltage window of 1.7–2.8 V (vs. Li/Li+). Shanghai Chenhua CH Electrochemical Workstation was used to test the electrochemical impedance spectra (EIS) and the impedance frequency was set at 100kHz to 0.01Hz. Cyclic voltammetry (CV) was

acquired in the range from 1.7 to 2.8 V. The lithium diffusion process can be described by the Randles-Sevcik equation:[2]

$$I_p = 2.69 \times 10^5 n^{1.5} A D_{Li^+}^{0.5} C_{Li^+} v^{0.5}$$

where I_p is the peak current, A; n is the number of electrons transfer, which is 2 for Li-S cells; A is the geometric area of the active electrode[3], cm^2. In this work, A is approximated as the electrode area [4, 5]; D_{Li^+} is the lithium ion diffusion rate, $cm^2\ s^{-1}$; C_{Li^+} is the concentration of Li^+ in the electrolyte, mol mL^{-1}; v is the scan rate, V s^{-1}.

The slope of the fitted line ($I_p/v^{0.5}$) reflects the lithium ion diffusion rate with all other parameters being constant namely n, A and C_{Li^+} as the peak current has a linear correlation with the square root of the scan rate.

5. Computational methods

Adsorption energies were calculated using Gaussian 09 software, which employs the density functional theory (DFT) method. To have a better discussion on the affinity of CMPA towards differing microscale LiPSs, the interactions of CMPA with a series of Lithium-polysulfides radicals at a molecular level were calculated. The geometries of the molecular were optimized through B3LYP/6-31+ basis set, followed by the adsorption energy calculation.

The adsorption energies of Li_2S_X ($1 \leq x \leq 8$) were defined as follow:

$$\Delta E_{ads} = E_{CMPA + Li_2S_x} - E_{CMPA} - E_{Li_2S_x}$$

where $E_{CMPA+Li_2S_x}$ is the electronic energy of the CMPA molecular with sulfur species which adsorbed on the CMPA molecular, E_{CMPA} is the electronic energy of the CMPA molecular, and $E_{Li_2S_x}$ is the electronic energy of Li_2S_x molecules. Based on this definition, a more negative value indicates a stronger binding system.

6. Preparation of Li_2S_6 solution

0.005 M Li_2S_6 (30 mM in sulfur) was prepared by chemically reacting sulfur with Li_2S in 1,3-dioxolane/1,2dimethoxyethane solution (DOL/DME, 1:1 by volume).

Supplementary Figures

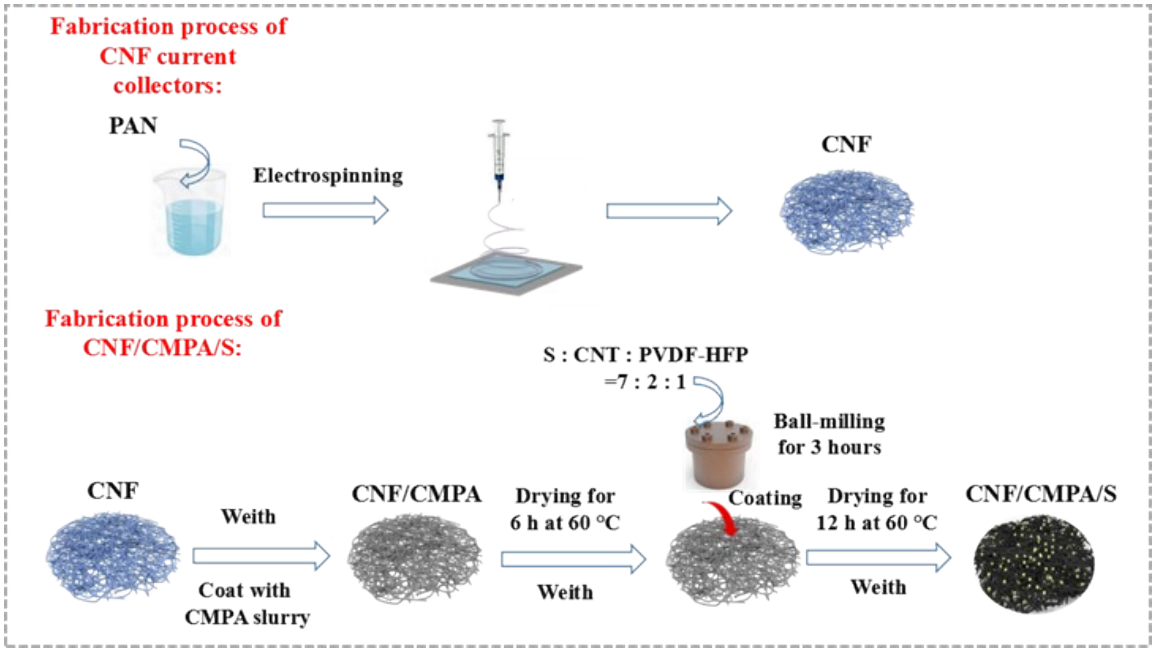

Fig. S1. Schematic illustration of the fabrication process of the CNF and CNF/CMPA/S.

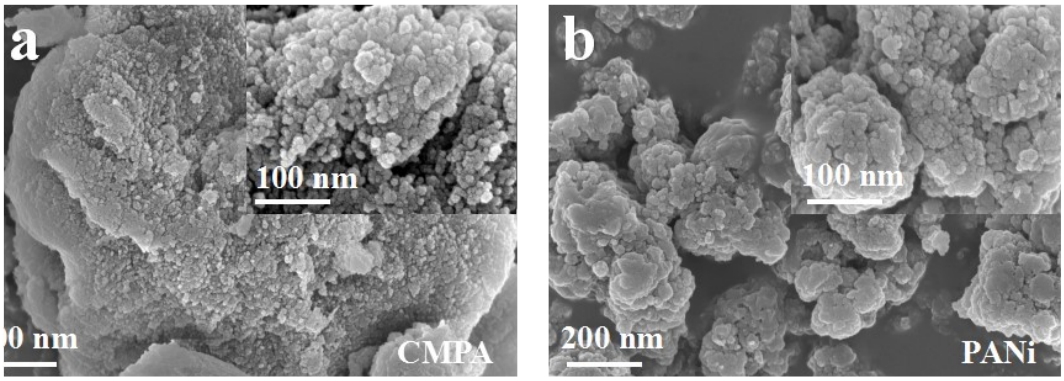

Fig. S2. SEM images of (a) CMPA and (b) PANi.

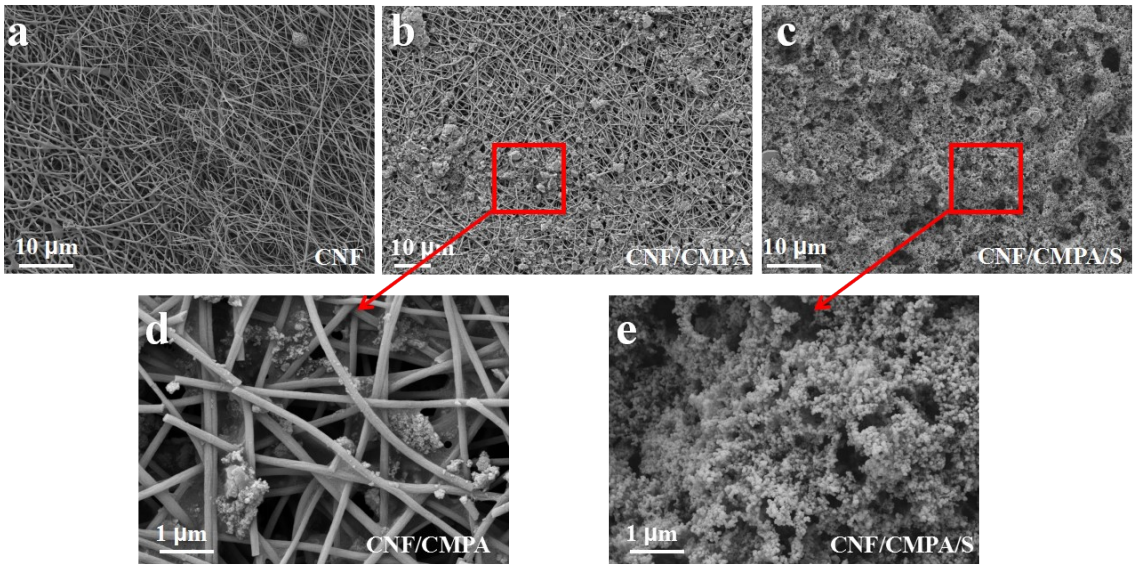

Fig. S3. SEM images (×1 K) of (a) CNF, (b) CNF/CMPA and (c) CNF/CMPA/S cathode. SEM images (×10 K) of (d) CNF/CMPA and (e)CNF/CMPA/S electrode.

As shown in Fig. S3b, CMPA is coated mainly onto the surface of CNF current collector, with part of CMPA slurry infiltrating into the free space of the 3D network under the effect of gravity (Fig. S3d). In Fig. S3c, the carbon nanofiber was covered with dense sulfur layer, supporting the three-layers structure of CNF/CMPA/S electrodes.

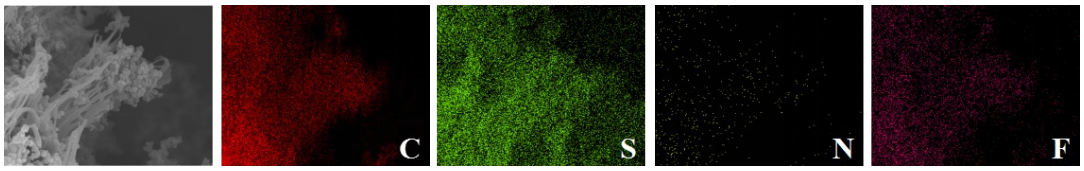

Fig. S4. EDS mapping of CNF/CMPA/S electrode.

The SEM mapping demonstrate that C, S, N and F elements coexist in the as-prepared CNF/CMPA/S cathode.

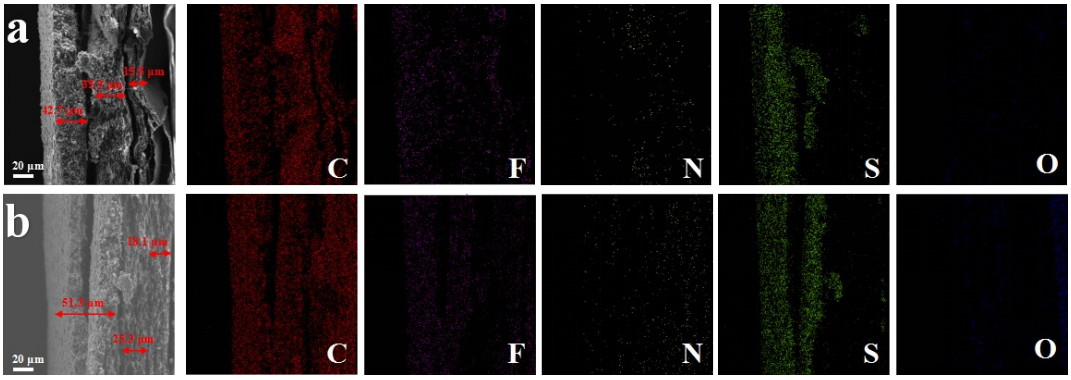

Fig. S5. Cross section SEM image and EDS mappings of the (a) CNF/CMPA/S and (b) CNF/PANi/S electrodes

Furthermore, cross-sectional SEM images (Fig. S5) show that the CNF/CMPA/S electrode functional layer (CNF/CMPA, thickness: ~50.8 μm) was in close contact with the sulfur layer (thickness: ~42.7 μm), and the differentiated elemental distribution corresponded well with the integrated structure of this CNF/CMPA/S electrode. The CNF/PANi/S electrode show the similar structure with PANi functional layer (thickness: ~25.3 μm) and the sulfur layer (thickness: ~42.7 μm).

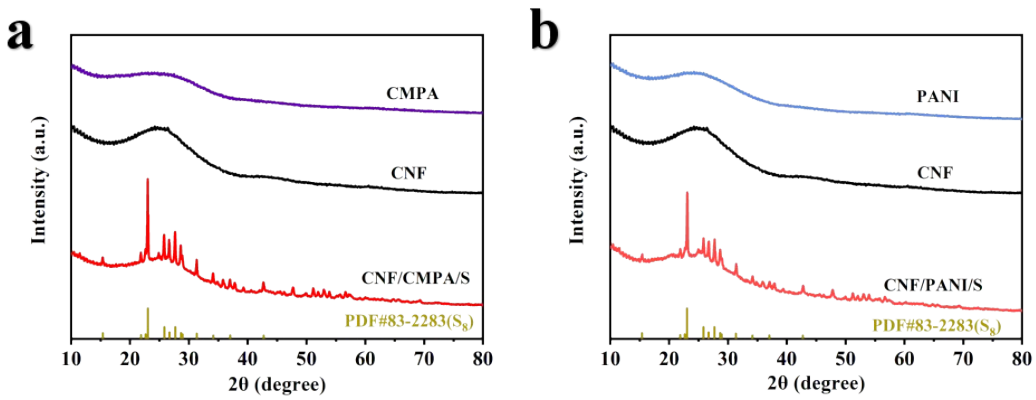

Fig. S6. XRD spectra of (a) CMPA, CNF and CNF/CMPA/S; (b) PANi, CNF and CNF/PANi/S.

X-ray diffraction (XRD) measurements in Fig. S6 indicates the representative amorphous nature of conducting polymer and carbon nanofibers. The typical S_8 diffraction peaks are found in the XRD curves of CNF/CMPA/S and CNF/PANi/S, proving the successful loading of active sulfur onto the modified current collectors.

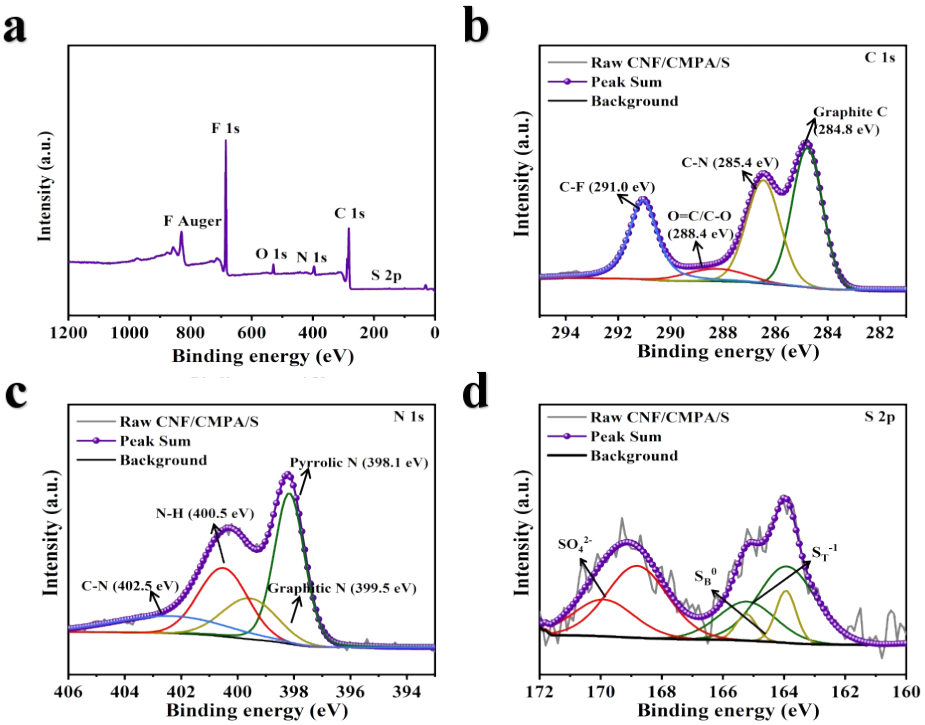

Fig. S7. High-resolution XPS spectra of (a) full spectrum, (b) C 1s (c) N 1p and (d) S 2p for CNF/CMPA/S electrode.

All the C, O, N, S and F elements are found in the XPS full spectrum of CNF/CMPA/S cathode in Fig. S7a, conforming to the previous EDS results. As shown in Fig. S7b, the refined C 1s XPS spectrum of CNT/CMPA/S cathode shows four characteristic peaks at 284.8 (Graphite C), 285.4 (C-N), 288.4 (O=C/C-O), and 291.0 eV (C-F), respectively [6]. The C-N bonds are created by the palladium-catalyzed cross-coupling of (aryl)amines with aryl halides [7] and the C-F bonds corresponding to the material structure of the binder PVDF-HFP. Moreover, the peaks in the N 1s spectrum of CNT/CMPA/S cathode (Fig. S7c) belong to the pyrrolic nitrogen (398.1 eV) in CMPA core, the graphitic nitrogen (399.5 eV) on CNF surface, the N-H species (400.5 eV) on the linker (phenylenediamine) of CMPA [7, 8] and the C-N bonding (402.5 eV) corresponding to PAN/CMPA, respectively [9]. The S 2p spectrum in Fig. S7d further shows three pairs of characteristic peaks at 163.8/165.0 (S_T^{-1}), 163.9/165.2 (S_B^0) and 168.8/170.0 (SO_4^{2-}) eV, deriving from the part that sulfur loaded on the current collector.

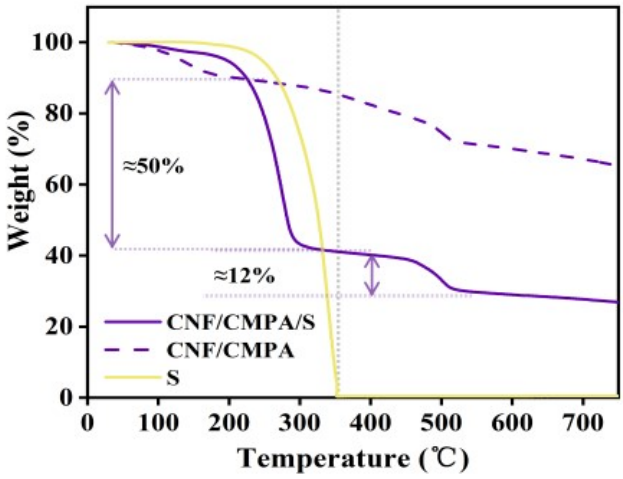

Fig. S8. TGA curve of the CNF/CMPA/S, CNF/CMPA and sulfur particles.

The thermogravimetric analysis (TGA) results are shown in Fig. S8, in order to assess the S contents of the high-loading cathodes. The pure S sample showed the start and end temperatures of S sublimation at 250 and 350 °C, respectively. The start and end temperatures of S sublimation in CNF/CMPA/S sample are 200 and 310 °C, respectively. Considering the mass loss of CMPA resulting from the stepwise thermal decomposition, the S concentration in the CNF/CMPA/S were further calculated to be approximately 50 wt%. The CMPA layer shows the start and end temperatures of S sublimation at 450 and 550 °C, respectively. Considering the mass loss of CMPA resulting from the stepwise thermal decomposition, the CMPA content in high-loading CNF/CMPA/S electrodes were further calculated to be approximately 12 wt%.

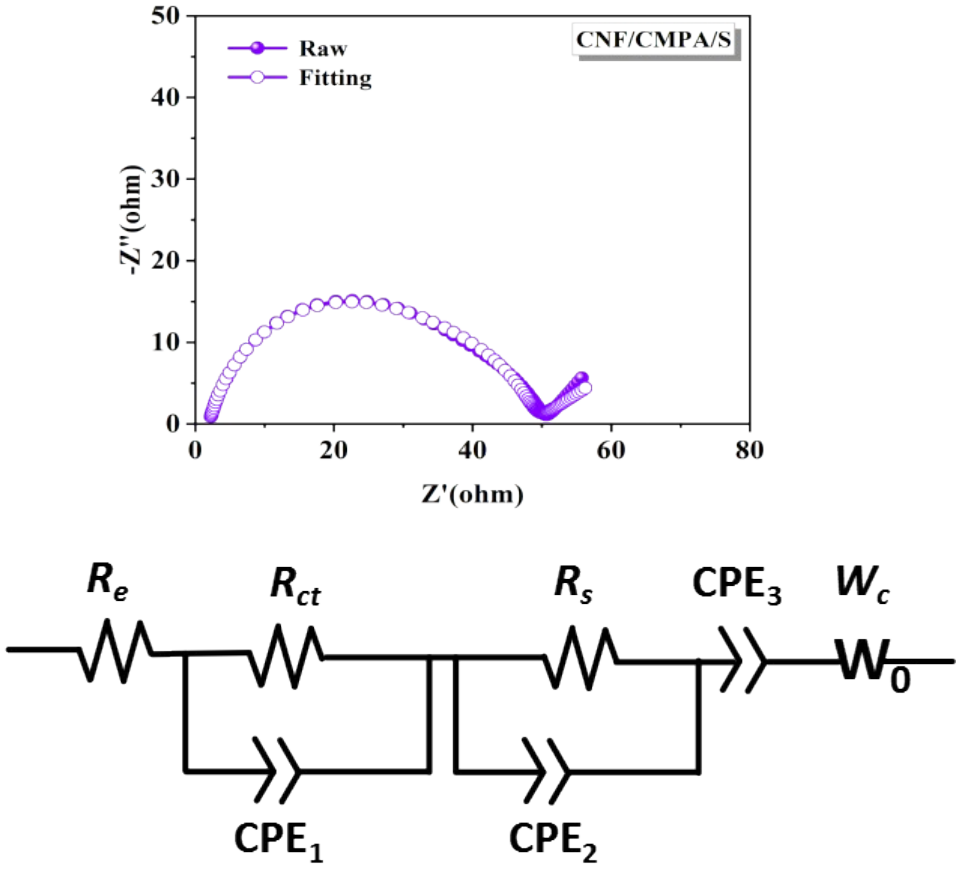

Fig. S9. Raw and fitted EIS curves of the CNF/CMPA/S electrode and equivalent circuit model.

All the Nyquist plots were composed by a high-frequency semicircle and a low-frequency sloped line, which are attributed to the charge transfer resistance (R_{ct}) and mass-diffusion process, respectively [1, 10].

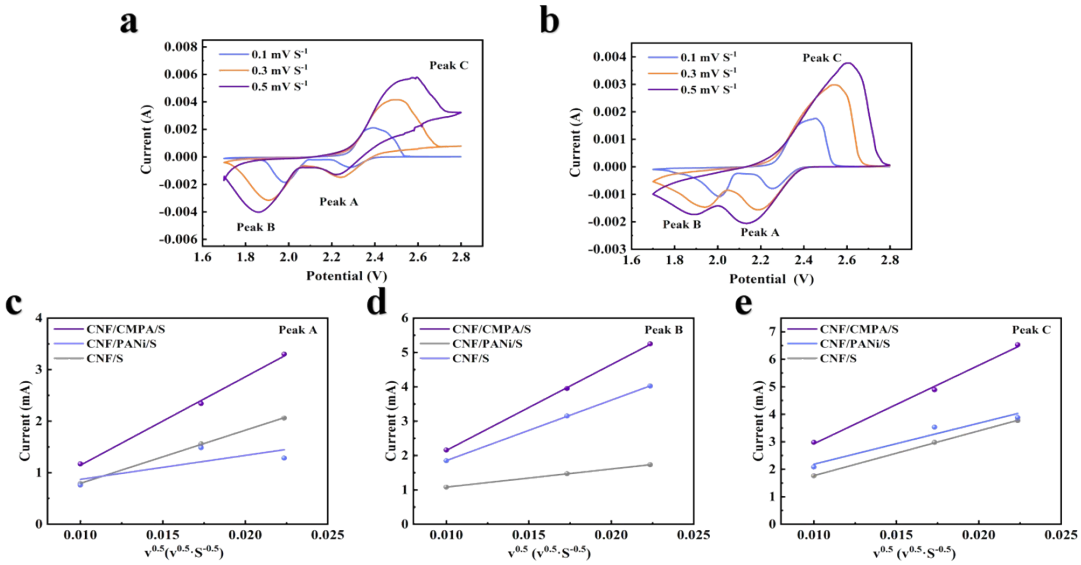

Fig. S10. CV plots of (a) CNF/PANi/S and (b) CNF/S electrodes at various scan rates ranging from 0.1 to 0.5 mV s^{-1}; Plots of CV peak current for the (c) first cathodic reduction process (peak A: $S_8 \rightarrow Li_2S_x$), (d) second cathodic reduction process (peak B: $Li_2S_x \rightarrow Li_2S_2/Li_2S$) and (e) anodic oxidation process (peak C: $Li_2S_2/Li_2S \rightarrow S_8$) versus the square root of the scan rates, according to the CV plots in Fig.3b and Fig. S10.

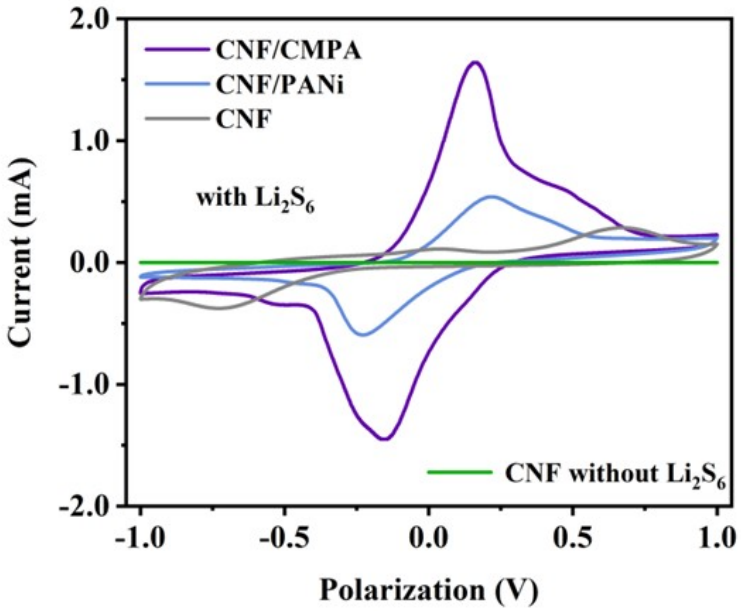

Fig. S11. CV curves of symmetric cells at 0.1 mV s^{-1}.

Fig. S11 shows the CV curves of CNF/CMPA, CNF/PANi and CNF symmetric batteries which illustrate the characteristic multistep sulfur redox processes. Among these samples, the CV curve of the CNF/CMPA symmetric batteries delivered a pair of redox peaks (-0.165/0.165 V) with the highest current. In contrast, the CNF/PANi electrode showed a lower redox peak than CNF/CMPA/S electrode. The CNF electrode exhibited a pair of broad peaks and a significantly reduced current density.

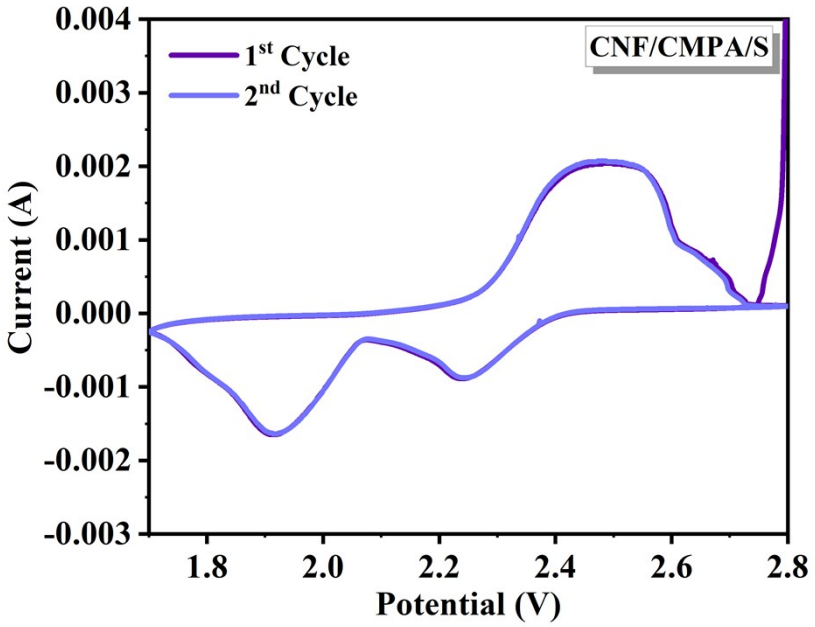

Fig. S12. CV plots of CNF/CMPA/S for the initial two cycles at 0.1 mV s^{-1} within a potential window of 1.7 V-2.8 V (vs. Li/Li^+).

The CV plots of CNF/CMPA/S cathode have two cathodic peaks at ~2.3 V (Peak A) and ~2.0 V (Peak B) which can be ascribed to the formation of the long-chain polysulfides (Li_2S_n, $3 \leq n \leq 8$) by S_8 reduction and the lithium sulfide (Li_2S_2 or Li_2S) by short-chain polysulfide reduction, respectively. The wide anodic peak located at ~2.4 V (Peak C) corresponds to the final oxidation products of elemental sulfur because of the oxidation of Li_2S and Li_2S_2. In addition, based on the initial CV curves of CNF/CMPA/S cathode in Fig. S12, the completely overlapped redox peaks suggest the high charging/discharging stability of the battery with CNF/CMPA/S cathode.

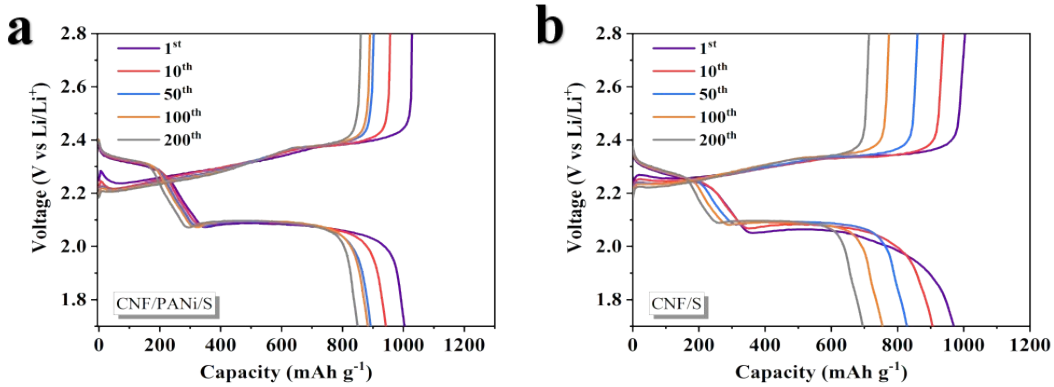

Fig. S13. The Charge/discharge profiles of (a) CNF/PANi/S and (b) CNF/S cathodes for 1st, 10th, 50th, 100th, and 200th cycles at 0.2C

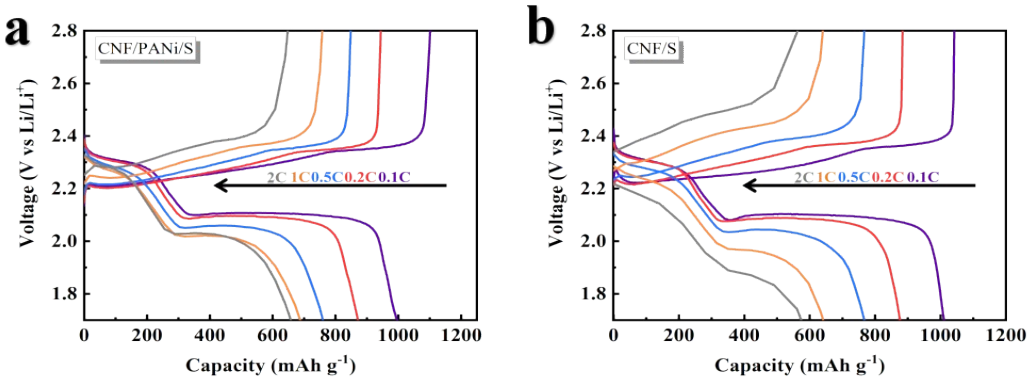

Fig. S14. The charge/discharge profiles of (a) CNF/PANi/S and (b) CNF/S at various current densities.

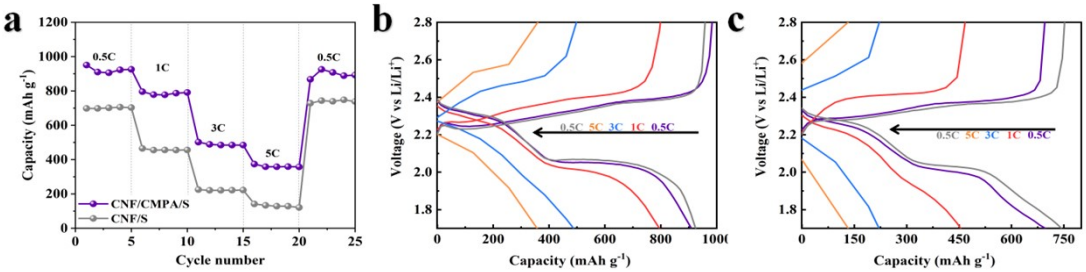

Fig. S15. The rate performances of CNF/CMPA/S and CNF/S electrodes at high current densities; The charge/discharge profiles of (b) CNF/CMPA/S and (c) CNF/S at various current densities.

The rate performance of CNF/CMPA/S and CNF/S electrodes at higher current density from 0.5 to 5 C were conducted, and the results are shown in Fig. S15. The CNF/CMPA/S electrode delivered the discharge capacities of 950.4, 795.4, 501.8, and 373.7 mAh g^{-1} at various rates of 0.5, 1, 3 and 5 C, respectively. A recovery capacity of 925.2 mAh g^{-1} can be achieved when the current density is resumed to 0.5 C. The CNF/CMPA/S electrode show more excellent electrochemical performance than CNF/S electrode at high current density (3C and 5C). However, both CNF/CMPA/S and CNF/S electrodes exhibit high polarization voltage at 3 C and 5 C (Fig. S15b and c).

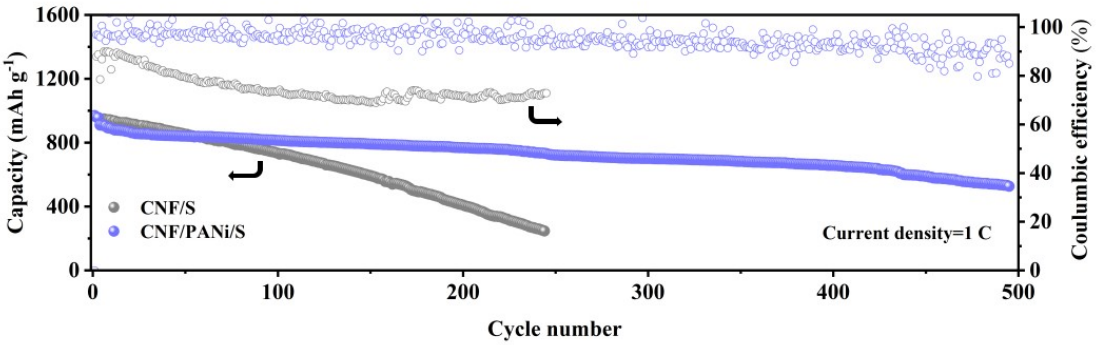

Fig. S16. Long-term cyclability of CNF/PANi/S and CNF/S electrodes.

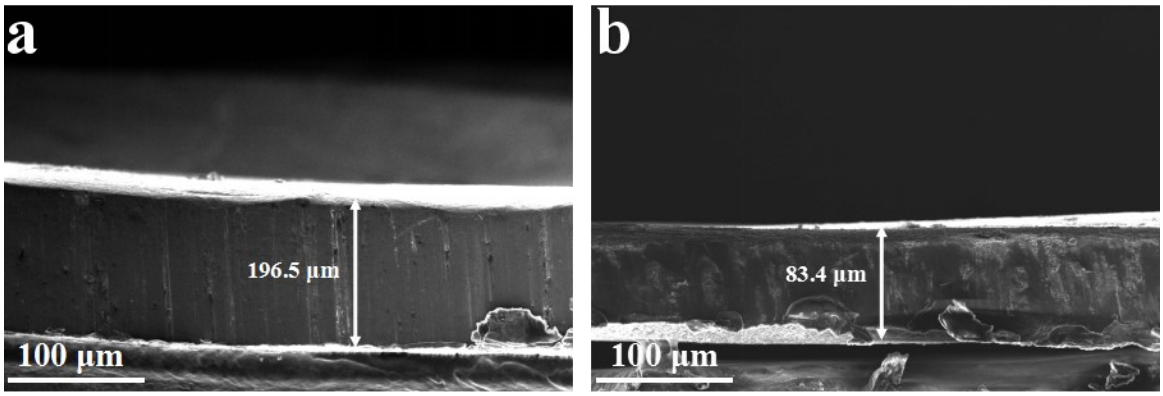

Fig. S17. SEM images of the cross-section of (a) ~200 µm and (b) ~80 µm thick lithium-metal foils.

The practical thickness for the defined 200 and 80 µm lithium-metal foils were 196.5 and 83.4 µm, respectively, measured by the own imaging analysis software of GeminiSEM500.

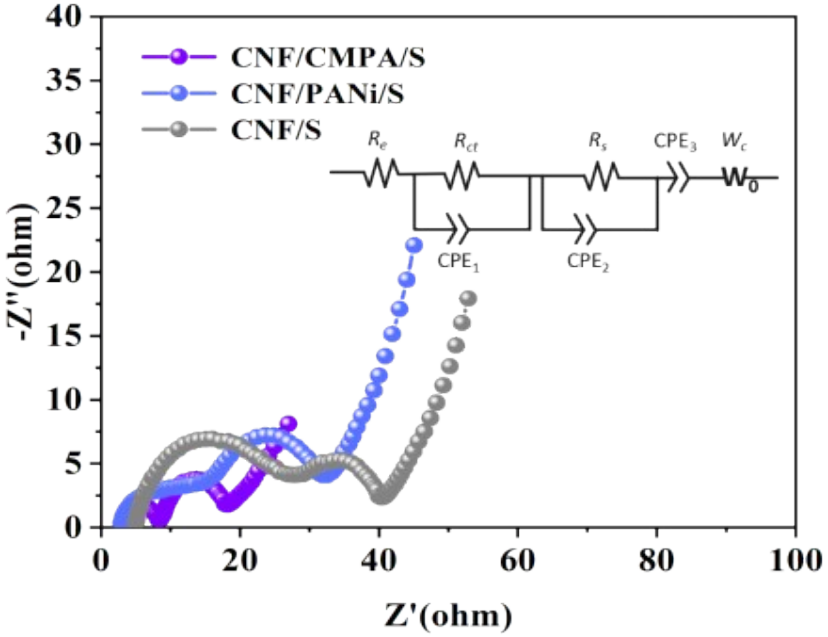

Fig. S18. EIS plot of the three electrodes tested at open-circuit voltage after 200 cycles.

EIS plots for various cathodes after 200 discharge/charge cycles are presented in Fig. S16. For CNF/CMPA/S electrode, the R_{ct} value gradually decreased from 44.53 Ω (fresh cell) to 9.19 Ω (200th cycle), demonstrating that the electrons transferring throughout the entire integrated system became more stable and smoother with increased cycle numbers [11, 12]. However, the R_s value gradually increased from 0.47 Ω (fresh cell) to 5.21 Ω (200th cycle), due to the thicker solid-electrolyte interface (SEI) film at the electrode surface with repeated cycling. In contrast, the CNF/PANi/S and CNF/S cathodes show high R_s value (13.89 Ω and 15.76 Ω, respectively). The lower resistance of CNF/CMPA/S cathode demonstrating smoother SEI film.

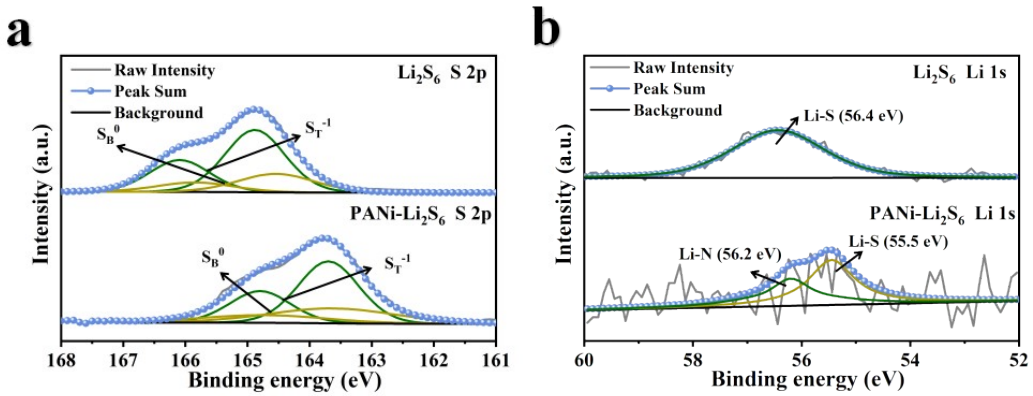

Fig. S19. XPS spectra of (a) S 2p and (b) Li 1s regions of pure Li_2S_6 molecule with and without addition of PANi.

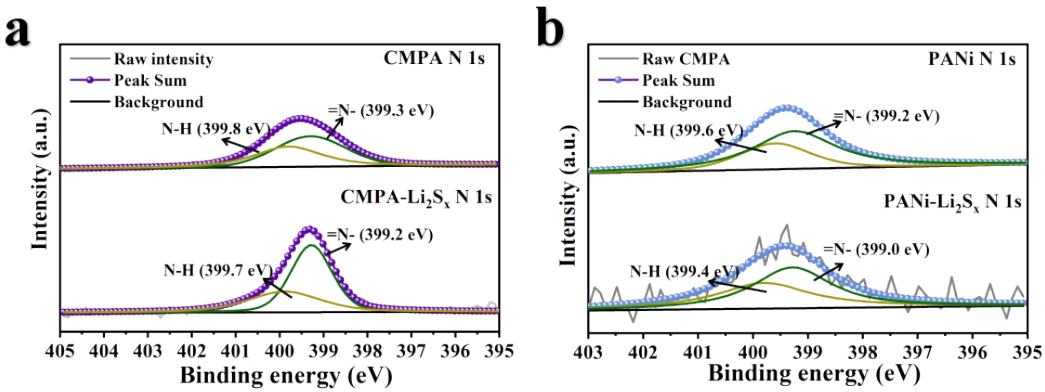

Fig. S20. XPS spectra of N 1s regions of (a) CMPA molecule and (b) PANi molecule before and after adsorbing Li_2S_6.

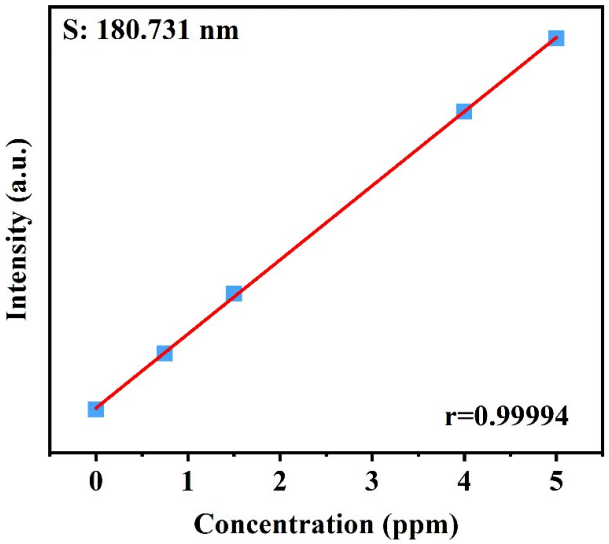

Fig. S21. Sulfur standard plot derived from ICP-AES;

The lithium metal anode was dissolved in 10 mL water and then used for ICP-AES analysis.

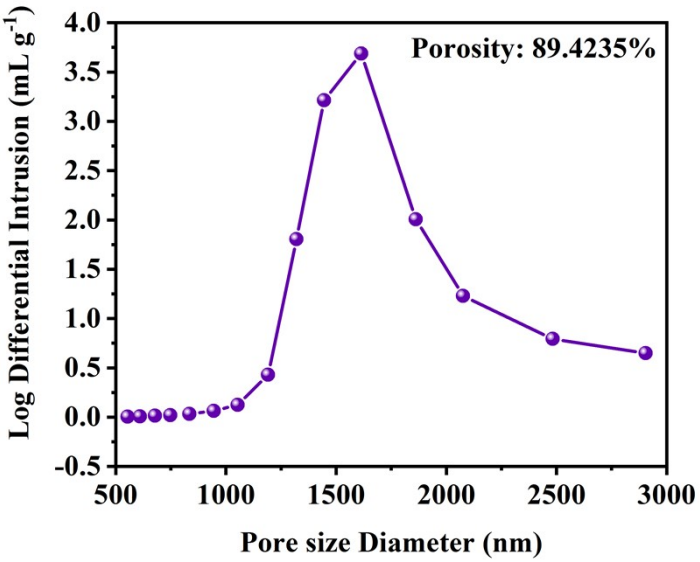

Fig. S22. The pore distribution of a) CNF/CMPA current collectors (mercury intrusion method).

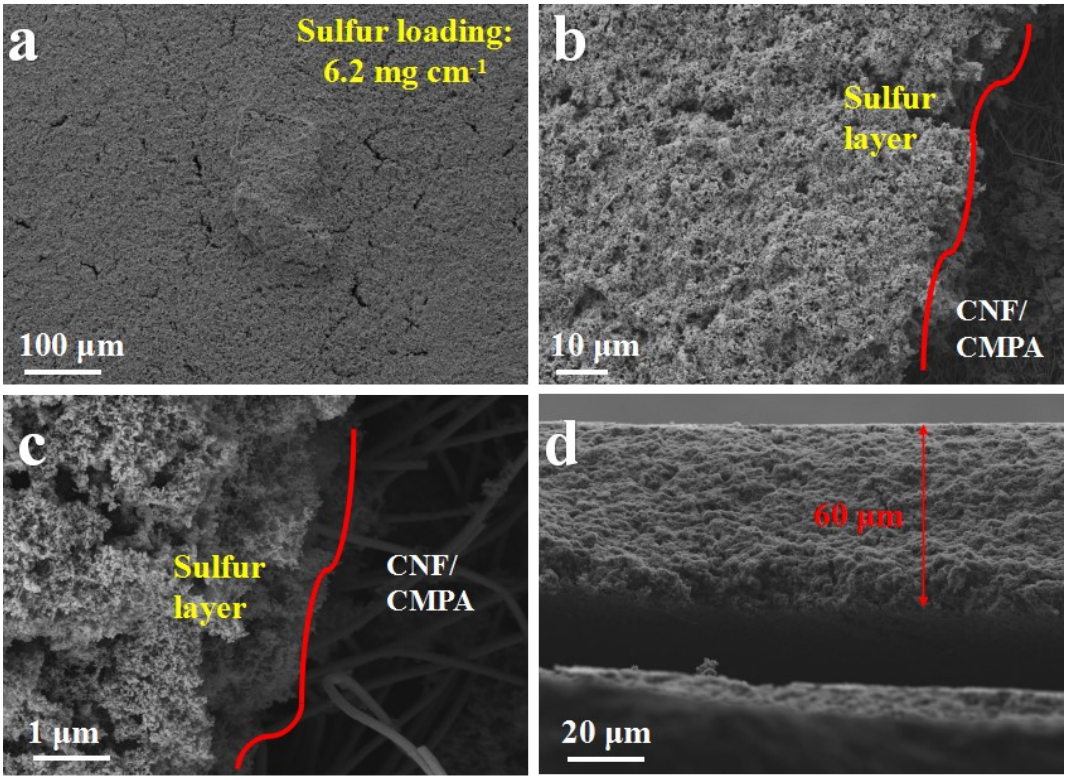

Fig. S23. The SEM images of CNF/CMPA/S electrode at high sulfur loading: (a) planform of electrode, (b) and (c) images of electrode boundary; (d) Cross section SEM image of CNF/CMPA/S electrode at high sulfur loading.

Fig. S23a proves that the active sulfur is homogeneously coated on the surface of current collectors. Fig. S23b and c support the hierarchical structure of CNF/CMPA/S electrodes. The cross section of CNF/CMPA/S electrode (Fig. S23d) shows a thicker sulfur layer (60 µm) compared with conventional electrodes (42.2 µm) in Fig. S5. Although a thicker layer of sulfur will introduce completely new dilemmas involving the cathode such as structural failure of electrode and severe "shuttle effect". But, the CMPA layer, acting as a buffer/protective layer of current collector, maintains the structure integrity of the cathode. Besides, CMPA with excellent conductivity will improve the catalytic conversion of sulfur and further increase the areal capacity.[13-16]

Supplementary Tables

Table S1 Detail information of XPS N 1s spectra of CMPA and PANi before and after adsorbing Li_2S_6 (According to the Fig. S18)

Assignment		CMPA			PANi		
		Peak position（eV）	**Peak area**	**Peak ratio**	**Peak position（eV）**	**Peak area**	**Peak ratio**
Before adsorption	=N−	399.3	481.1	**0.583**	399.2	581.2	**0.560**
	N−H	399.8	343.1	0.417	399.6	457.3	0.440
After adsorption	=N−	399.2	2044.2	**0.618**	399.0	469.5	**0.649**
	N−H	399.7	1263.3	0.382	399.4	253.3	0.351

Table. S2 Impedance data calculated from EIS results shown in Fig. 3d

Batteries	Re (Ω)	Rct (Ω)	Rs (Ω)	Measurement errors
CNF/CMPA/S	1.99	44.53	0.47	≤4.104 pct
CNF/PANi/S	5.09	40.26	3.38	≤1.588 pct
CNF/S	5.82	157.70	0.70	≤1.688 pct

Table. S3 Impedance data calculated from EIS results shown in Fig. S16

Batteries	Re (Ω)	Rct (Ω)	Rs (Ω)	Measurement errors
CNF/CMPA/S	3.58	9.20	5.22	≤1.154pct
CNF/PANi/S	2.28	13.44	13.89	≤3.397 pct
CNF/S	4.79	20.24	15.76	≤ 2.587pct

Table. S4 Comparisons of the lithium-ion diffusion rate (D_{Li+}) of three as-prepared cathodes.

Batteries	Lithium-ion diffusion rate D_{Li}^{+} (cm^2 S^{-1})		
	Peak A	**Peak B**	**Peak C**
CNF/CMPA/S	2.36×10^{-8}	4.67×10^{-8}	6.69×10^{-8}
CNF/PANi/S	5.22×10^{-9}	2.29×10^{-8}	6.38×10^{-8}
CNF/S	8.00×10^{-9}	2.05×10^{-9}	2.00×10^{-8}

Table. S5 Comparison of the discharge specific capacities of cathodes modified by conducting polyaniline at various current densities with those of other reported materials.

Materials	Reversible capacity (mA h g^{-1})					Reference
	0.1 C	0.2 C	0.5 C	1 C	2 C	
S@PANi/GO composite cathode	1027	917	810	714	613	44
CPANiP-NaCl/Sulfur cathode	812	706	565	492	419	45
C-PANi/S@PDA composite cathode with MWCNT/SPANI-coated separator	988	868	848	715	546	18
cp(S-g-PANi)/S (SPAS) cathode	1150	1000	900	790	550	46
PANi-DSMC-SeS_2 cathode	1002	938	820	717	619	47
nanotube PANi-S	1088	692	521	440	421	48
nano-microsphere PANi-S	885	523	334	236	186	48
PPy@S@GA cathode	1186	978	879	778	755	49
CNF/CMPA/S cathode	1047	978	905	855	785	This work

Table. S6 Calculations of the N/P ratio in the conventional Li-S coin and high-loading coin assembled by CNF/CMPA/S cathodes.

Batteries-Li thickness（μm）	Cathode (PE)				Anode (NE)				N/P ratio
	Electrode area（cm^2）	Active material loading ($mg\ cm^{-2}$)	Areal specific($mA\ h\ cm^{-2}$)	specific capacity (mA h)	Electrode area（cm^2）	Active material loading ($mg\ cm^{-2}$)	Areal specific($mA\ h\ cm^{-2}$)	specific capacity (mA h)	
Li-S coin battery-200(Low S loading)	1.54	0.98	1.64	2.53	2.01	10.68	41.22	82.86	32.78
Li-S coin battery-200(High S loading)	1.54	7.38	12.36	19.04	2.01	10.68	41.22	82.86	4.35
Li-S coin battery-80	1.54	8.72	14.61	22.49	2.01	4.539	17.52	35.22	1.57

*The defined specific capacity is 1675 mAh g^{-1} for sulfur and 3860 mAh g^{-1} for lithium. The diameters of the cathode and the anode discs in the coin batteries were fixed to be 14 and 16 mm, respectively [12].

Table. S7 Calculations of the areal weight and gravimetric energy density for various Li-S batteries.

Batteries-Li thickness（μm）	Current collector (mg cm^{-1})	CMPA layer (mg cm^{-1})	Active layer (mg cm^{-1})	Separator (mg cm^{-1})	Electroly-te (mg cm^{-1})	Li anode (mg cm^{-1})	Total weight (mg cm^{-1})	Intail capacity (mAh g^{-1})	Gravim-etric energy density (Wh Kg_{cell}^{-1})
Li-S coin battery-200(Low S loading)	1.64	0.39	1.40	1.24	28.00	10.68	43.35	1074.10	52.2
Li-S coin battery-200(High S loading)	1.86	1.91	10.55	1.24	67.20	10.68	93.44	958.20	162.7
Li-S coin battery-80	1.52	2.90	12.46	1.24	56.00	4.54	78.66	851.55	202.8

*The mass of electrolyte is measured to be 1.12 mg uL^{-1}; The density of Li anode is 0.534 g cm^{-3}; The mass ratio of the active sulfur to the whole active layer was 70%.

In Fig. 4g and Table. S7, the area weights of various components in conventional Li-S battery (this work), high-loading Li-S battery (~200 μm Li) and high-loading Li-S battery (~80 μm Li) were provided. The conventional Li-S batteries which investigated previously in Fig. 3 with low sulfur areal loading (<2.0 mg cm^{-2}) and a high E/S ratio (>30 mL g^{-1}). Li–S cells that combine high sulfur loading in the cathode and a polysulfide-based catholyte with low electrolyte-to-sulfur ratios provide a promising route to practical batteries with high specific energies. In this work, to evaluate the performance of CMPA functional layer in practical Li-S batteries, the Li-S cells were assembled by a CNFs current collector with high sulfur areal loading, and a thinner lithium anode and a lower E/S ratio. In addition, lithium foils with different thickness

(~200 μm and even 85 μm) were tested as the anode to further control the N/P ratio of batteries, as shown in Table S5.

The cell-level gravimetric energy density values for Li-S coin battery-200 and Li-S coin battery-80 were also calculated based on the whole basic units of battery system (neglecting the mass of any packaging material), as shown in the following formula:

$$\frac{Capacity\ mAh\ g^{-1} \times 2.15\ V \times mass(S)\ mg\ cm^{-2}}{(m_{curreny\ collector} + m_{Functional\ layer} + m_{Active\ layer} + m_{Electrolyte} + m_{Separat}}$$

The calculation results are shown in the fig. 5g and table. S6.

The cell-level gravimetric energy density value (1st cycle) for conventional Li-S coin battery-200: 1074.10×2.15×1.4×70%/55.87=52.2 Wh Kg_{cell}^{-1}

The cell-level gravimetric energy density value (1st cycle) for high-loading Li-S coin battery-200: 958.20×2.15×10.55×70%/93.44=162.7 Wh Kg_{cell}^{-1}

The cell-level gravimetric energy density value (1st cycle) for high-loading Li-S coin battery-80: 851.55×2.15×12.46×70%/78.66=202.8 Wh Kg_{cell}^{-1}

Notably, for the high loading of the Li-S batteries, the low E/S ratio and thin lithium anode is critical for reducing the total battery weight and consequently achieving a high cell-level gravimetric energy density [12, 17].

Table. S8 Comparison of the areal capacity of CNF/CMPA/S at a high sulfur loading with that of other conducting polymer materials reported in previous.

Materials	Sulfur loading (mg cm^{-2})	Current density (mA cm^{-2})	Initial areal capacities (mA h cm^{-2})	Areal capacities after cycling (mA h cm^{-2})	Reference
PANi/S	3.97	0.44	1.99	3.57	50
S-g-PANi@S	2	0.22	2.30	1.47	46
MWCNT/sPANi	5	0.33	5.63	4.57	18
SPANi@N-GO/CNT	1.6	0.32	1.91	1.15	51
CNF/S/PANi	2	0.45	1.26	1.42	52
PANi/S	2	0.22	1.81	1.00	56
S/PSKC/PPy	2	0.34	2.22	1.86	57
PSS/PPy	6	0.67	6.65	4.22	58
CNF/CMPA/S(convention)	1.4	0.47	1.50	1.32	This work
CNF/CMPA/S(200 μm Li)	7.38	0.82	7.01	6.21	This work
CNF/CMPA/S(80 μm Li)	8.72	0.97	7.42	5.23	This work

Table. S9 Calculations of the sulfur content of the conventional and high sulfur-loading CNF/CMPA/S electrodes.

Batteries-Li thickness (μm)	Carbon nanofiber (mg)	CMPA layer (mg)	Active layer (mg)	Mass of sulfur （mg）	Mass of electrode （mg）	Sulfur content (%)
Li-S coin battery-200(Low S loading)	2.53	0.60	2.15	1.51	5.28	28.49
Li-S coin battery-200(High S loading)	2.86	2.94	16.25	11.38	22.05	51.59
Li-S coin battery-80	2.34	4.47	19.19	13.43	26.00	51.67

Table. S10 Calculations of the CMPA content of the conventional and high sulfur-loading CNF/CMPA/S electrodes.

Batteries-Li thickness （μm）	Carbon nanofiber (mg)	CMPA layer (mg)	Active layer (mg)	The CMPA content (%)
Li-S coin battery-200 (Low S loading)	2.53	0.60	2.15	11.36
Li-S coin battery-200 (High S loading)	2.86	2.94	16.25	13.33
Li-S coin battery-80	2.34	4.47	19.19	17.19

To obtain accurate values of CMPA contents in CNF/CMPA/S electrodes, the mass of the electrode was measured at each fabrication stage. The detailed mass of components of CMPA/CNF/S electrodes were conducted in table. S10 to show the CMPA content of electrodes. Notably, the content of CMPA was increased under high loading conditions in order to fix more active sulfur.

References

1. J. Wang, G. Yang, J. Chen, Y. Liu, Y. Wang, C. Y. Lao, K. Xi, D. Yang, C. J. Harris, W. Yan, S. Ding and R. V. Kumar, *Adv. Energy Mater.*, 2019, **9**, 1902001.
2. G. Zhou, H. Tian, Y. Jin, X. Tao, B. Liu, R. Zhang, Z. W. Seh, D. Zhuo, Y. Liu, J. Sun, J. Zhao, C. Zu, D. S. Wu, Q. Zhang and Y. Cui, *Proc. Natl. Acad. Sci. U. S. A.*, 2017, **114**, 840-845.
3. P. Yu, F. Wang, T. A. Shifa, X. Zhan, X. Lou, F. Xia and J. He, *Nano Energy*, 2019, **58**, 244-276.
4. W. G. Lim, C. Jo, A. Cho, J. Hwang, S. Kim, J. W. Han and J. Lee, *Adv. Mater.*, 2018, **31**, 1806547.
5. Y. Zhang, X. Liu, L. Wu, W. Dong, F. Xia, L. Chen, N. Zhou, L. Xia, Z.-Y. Hu, J. Liu, H. S. H. Mohamed, Y. Li, Y. Zhao, L. Chen and B.-L. Su, *J. Mater. Chem. A*, 2020, **8**, 2741-2751.
6. Y. Zhan, H. Yu, L. Ben, Y. Chen and X. Huang, *Electrochim. Acta*, 2017, **255**, 212-219.
7. J. Chen, Y. Wang, C. Ye, W. Lyu, J. Zhu, W. Yan and T. Qiu, *ACS Appl. Mater. Interfaces*, 2020, **12**, 28681-28691.
8. J. Chen, W. Yan, E. J. Townsend, J. Feng, L. Pan, V. Del Angel Hernandez and C. F. J. Faul, *Angew Chem Int Ed Engl*, 2019, **58**, 11715-11719.
9. P. Jia, T. Hu, Q. He, X. Cao, J. Ma, J. Fan, Q. Chen, Y. Ding, J. Pyun and J. Geng, *ACS Appl. Mater. Interfaces*, 2018, **11**, 3087-3097.
10. J. Liu, J. Wang, L. Zhu, X. Chen, Q. Ma, L. Wang, X. Wang and W. Yan, *Chem. Eng. J.*, 2021, **411**, 128540.
11. Y. Wang, R. Zhang, J. Chen, H. Wu, S. Lu, K. Wang, H. Li, C. J. Harris, K. Xi, R. V. Kumar and S. Ding, *Adv. Energy Mater.*, 2019, **9**, 1900953.
12. J. Wang, S. Yi, J. Liu, S. Sun, Y. Liu, D. Yang, K. Xi, G. Gao, A. Abdelkader, W. Yan, S. Ding and R. V. Kumar, *ACS Nano*, 2020, **14**, 9819-9831.
13. X. Yang, X. Gao, Q. Sun, S. P. Jand, Y. Yu, Y. Zhao, X. Li, K. Adair, L. Y. Kuo, J. Rohrer, J. Liang, X. Lin, M. N. Banis, Y. Hu, H. Zhang, X. Li, R. Li, H. Zhang, P. Kaghazchi, T. K. Sham and X. Sun, *Adv. Mater.*, 2019, **31**, 1901220.
14. J. Zhou, T. Wu, Y. Pan, J. Zhu, X. Chen, C. Peng, C. Shu, L. Kong, W. Tang and S. L. Chou, *Adv. Funct. Mater.*, 2021, 2106966.
15. Y. Hu, W. Chen, T. Lei, Y. Jiao, J. Huang, A. Hu, C. Gong, C. Yan, X. Wang and J. Xiong, *Adv. Energy Mater.*, 2020, **10**, 2000082.
16. R. Fang, S. Zhao, P. Hou, M. Cheng, S. Wang, H.-M. Cheng, C. Liu and F. Li, *Adv. Mater.*, 2016, **28**, 3374-3382.
17. J. Liu, J. Wang, L. Zhu, X. Chen, Q. Ma, Z. Xu, S. Sun, N. Wang, Q. Chai and W. Yan, *J. Colloid. Interface Sci.*, 2022, **606**, 1111-1119.